Nano Energy 104 (2022) 107887

Contents lists available at ScienceDirect

Nano Energy

journal homepage: www.elsevier.com/locate/nanoen

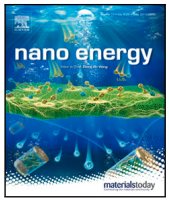

Full paper

Energy and dynamic analysis of quasi-static toggling mechanical energy harvester

Shiyi Liu [a], Xin Li [b], Li Teng [a], Guobiao Hu [c], Junrui Liang [a,*]

[a] School of Information Science and Technology, ShanghaiTech University, Shanghai 201210, China
[b] Guangzhou Institute of Technology, Xidian University, Guangzhou, Guangdong, China
[c] Internet of Things Thrust, The Hong Kong University of Science and Technology (Guangzhou), Guangzhou, Guangdong 511400, China

ARTICLE INFO

Keywords:
Electromagnetic energy harvester
Self-powered wireless switch
Potential energy precharging
Frequency up-conversion
Bistable structure

ABSTRACT

The self-powered wireless switch is one of the successful battery-free electronic products, which can be fully powered by a small mechanical energy harvesting (MEH). In most existing designs, bistable toggling electromagnetic energy harvesters are utilized to extract the mechanical energy associated with the switch toggling motions. Although such MEH modules are already put into volume production, the toggling dynamics and their energy profile have not been seriously investigated yet. This paper gives a comprehensive study of this toggling MEH. The released energy in a toggling action is quantified based on a varying potential well theoretical model. The mechanical–magnetic–electrical interaction within this dynamic system is better revealed with a simulation model built in Matlab Simulink. Experimental results further validate both the theory and simulation. The new insight into these quasi-static MEH systems and their essential potential energy precharging mechanism fills the gap between leading engineering practice and lagging academic study, in terms of application significance, over the last two decades.

1. Introduction

Mechanical energy harvesting (MEH) technology is developed with the purpose to scavenge energy from ambient mechanical sources, then using the harvested energy to power the pervasively distributed Internet of Things (IoT) devices, i.e., turning the otherwise wasted mechanical energy into useful information [1–5]. The ambient vibrations or motions usually cover some relative low-frequency spectrum, e.g., below 100 Hz. Many sophisticated frequency up-conversion techniques have been proposed by scholars from academia for transferring the energy concentrated in the low-frequency band to the high-frequency one, which better matches the resonant frequencies of most rigid MEH structures [6–10]. However, industrial engineers prefer simpler and more practical designs to manufacture their products. The motion-powered toggling wireless switch is a good example. One of the earliest products was released by EnOcean GmbH from Germany around 2001 [11,12]. Fig. 1(a) and (b) show the EnOcean ECO 200 MEH module and its explosive view, respectively. Many manufacturers, e.g., the ZF Group from Germany [13], Alps. Ltd. from Japan [14], Linptech Ltd. from China [15], and Chlorop Ltd. also from China [16], have released similar self-powered switch products.

The aforementioned commercial MEH modules for the self-powered wireless switches are all based on the instantaneous magnetic poles swapping principle [12]. These toggling switches have a significant common feature that they can work under extremely low-frequency or slow excitations. To be more professional, such excitations can be referred to as *quasi-static* motions. The triggering behavior of these quasi-static toggling (QST) MEH is very similar to those in the snap-through or bistable designs [17]. Yet, most of the previous studies of snap-through and bistable structures considered the performance in bandwidth broadening by directly exerting continuous vibration excitations to them [7–9]. The detailed transient dynamics and energy profile in each triggering motion were not thoroughly investigated. On the other hand, from the successful application of the motion-powered switches [11] and other transient-motion exciting designs [18], it turns out that, only one QST action is good enough to provide sufficient energy for the sub-1G or Bluetooth wireless transmission. Although these QST devices have already experienced booming growth in the industry and been put into a successful business over the last two decades, such a concept of QST-MEH has not caught sufficient attention and emphasis in the academic community. Only a few papers studied the behavior of some post-buckling mechanical structures and used the concept of quasi-static excitation until now [19,20]; the understanding is far from a systematic insight toward a battery-free IoT system energized by the harvested energy from a quasi-static motion.

* Corresponding author.
E-mail address: liangjr@shanghaitech.edu.cn (J. Liang).

https://doi.org/10.1016/j.nanoen.2022.107887
Received 27 July 2022; Received in revised form 19 September 2022; Accepted 9 October 2022
Available online 13 October 2022

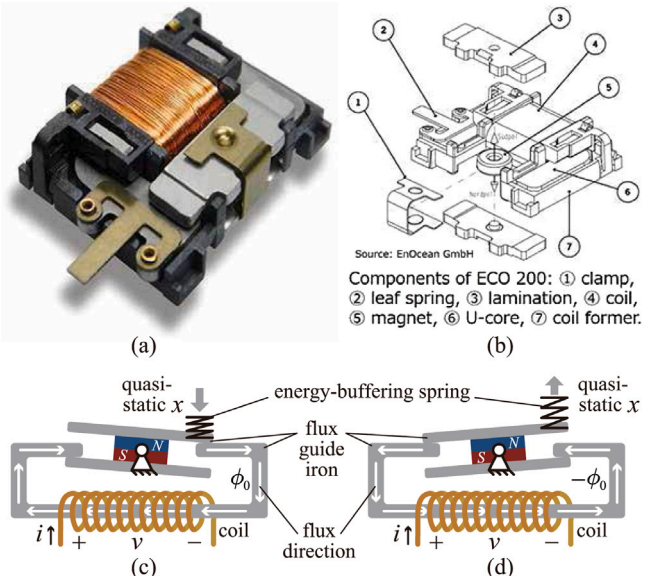

Fig. 1. Quasi-static motion energy harvester (ECO 200 by EnOcean GmbH). (a) Harvester module. (b) Explosive view [11]. (c) and (d) Schematics showing the two stable positions after two toggling steps.

This paper gives a comprehensive investigation of the QST-MEH system by studying its mechanical–magnetic–electrical coupling dynamics and energy flow. The previous analytical approaches for the continuously excited frequency up-conversion, snap-through, bistable, or multi-stable structures become invalid for describing a single QST motion. A varying potential well model is thus developed to analytically study the energy accumulating and releasing process in each QST action. The dynamics after toggling are numerically analyzed with a mechanical–magnetic–electrical multifield coupling model built in Simulink.

2. Working principle at a glance

The existing QST-MEH structures were mostly designed based on engineering experiences without rigorous theoretical modeling and parametric analysis. Two mechanisms, namely, *instantaneous magnetic poles swapping* and *potential energy precharging*, respectively, enable and enhance the MEH effect.

2.1. Instantaneous magnetic poles swapping

The key mechanism enabling the QST-MEH design is based on the instantaneous magnetic poles swapping technique [12], whose principle is illustrated in Fig. 1(c) and (d). The moving part of the QST harvester is a seesaw-like magnet and magnetic flux guide iron bars assembly. As it toggles in between the clockwise [Fig. 1(c)] and counterclockwise [Fig. 1(d)] stable positions, the magnetic flux flowing through the coil changes between ϕ_0 to $-\phi_0$. According to Faraday's Law of induction, a pulsed electromotive force (EMF), i.e., voltage or potential difference, will be induced in the coil during a rapid magnetic pole swapping transition.

2.2. Potential energy precharging

Besides the toggling magnetic structure, in almost all designs, the triggering bar is driven by an additional spring, which might be a leaf spring or spiral spring [12]. Such an auxiliary component is essential, as it can significantly enhance the harvested power. The secret results from the accumulated strain energy associated with its deformation before breaking through the magnetic adhesion. Therefore, this auxiliary spring is called the *energy-buffering spring* in this study, which is illustrated in Fig. 1. The mechanism of potential energy precharging has caught some research interest recently [18]. The idea is not unprecedented but very useful, in particular, for energy harvesting from quasi-static motions or extremely low-frequency vibrations. Because the potential energy does not rely on the frequency or speed of a movement. By accumulating or buffering mechanical energy from a motion, regardless of its speed, and later releasing it in a burst mode, the electromechanical energy transformation efficiency can be robustly guaranteed. In particular, for electromagnetic generators, the EMF in electromagnetic induction is proportional to the changing rate of magnetic flux. The more and faster the magnetic flux changes, the higher and easy-to-process voltage can be generated from an electromagnetic generator. It compensates for the drawback of a linear electromagnetic generator, which usually produces a relatively large current but small voltage output, compared to other MEH mechanisms, such as piezoelectric and triboelectric ones [21,22].

Although it was mostly seen that the MEH technology was referred to as kinetic energy harvesting (KEH). But obviously, with the successful application of the potential energy precharging mechanism in the QST switches, the harvester that scavenges energy from ambient vibrations or motions should be more accurately and generally referred to as a mechanical or motion energy harvester.

The theoretical fundamentals of potential energy precharging in the QST-MEH structure will be discussed in detail in the following parts of this article.

2.3. Special and valuable features

As one of the commercialized small MEH modules, which was put into volume production, the QST electromagnetic harvesters have some significant features compared with other MEH designs, which are summarized as follows:

- *Excellent frequency up-conversion capability*. The QST action is activated and sends out a voltage pulse whenever the moving part passes the critical positions, regardless of the moving speed or frequency.
- *Relative high output voltage*. Most commercial QST harvester's maximum instant output voltage can be up to 20 V, which is much higher than many linear or frequency up-conversion electromagnetic MEH designs.
- *Quantifiable input mechanical energy*. The quasi-static exciting case ensures the lowest amount of input energy in each toggling; excitation at a higher speed gives a larger amount of energy. This feature is unique and useful for ensuring a successful wireless transmission along with each toggling action.
- *Reliable operation*. From the testing data of the manufacturer, the compact QST-MEH module can be effectively toggled for more than one million times [11,14].

Although the QST-MEH modules have such unique features and already had been put into a successful business for two decades, a comprehensive study of their dynamics and energy flow is still absent. This paper is targeted to fill this gap between leading engineering practice and lagging academic research.

3. Theoretical energy analysis

A theoretical lumped mechanical model is developed to evaluate the amount of input mechanical energy during the energy accumulation and releasing process under quasi-static excitations.

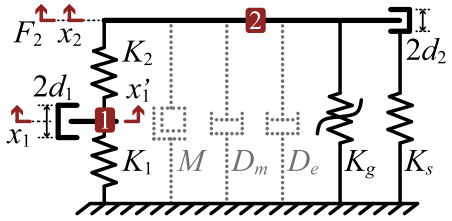

Fig. 2. Lumped model. (The dashed dynamic components play no effect before each quasi-static toggling action.)

3.1. Quasi-static model

Fig. 2 shows the equivalent lumped model of the QST-MEH module. The effect of toggling magnetic structure is abstracted by a nonlinear stiffness K_g and a two-way stopper, whose gap is a constant $2d_2$ and contact stiffness is K_s. K_2 represents the energy-buffering spring, while K_1 is the rebounding spring for monostable design. The magnet-iron moving assembly is represented as node 2, whose displacement is x_2. The action point is denoted as node 1, whose displacement is x_1'. Given that each toggling action only applies a unidirectional force to the action point, such a mechanism is modeled with a moving stopper, whose gap is a constant $2d_1$ and displacement is x_1. To distinguish x_1 and x_1' is necessary because, in some cases, the action point might fly out of the finger after passing the critical position. The aforementioned springs and stoppers form the toggling mechanism and determine the input energy. For the dynamics after toggling, the dynamic components, such as equivalent mass M, mechanical damper D_m, and electrically induced damper D_e, which results from energy extraction, should be taken into account [23,24]. In this study, the theoretical model only considers the quasi-static energy process. Since the dynamics after an energy-releasing instant involve complex interactions such as collision and mechanical–magnetic–electrical coupling, they are studied with numerical simulation in Section 4.

The total force applied at node 2 reflects the state of the QST harvester, in particular, the conditions before and after the critical toggling positions. This force is formulated as follows

$$\begin{aligned} F_2(x_1,x_2) =& F_{K2}+F_{Kg}+F_{Ks} \\ =& -K_2\left(x_2-x_1'+x_{20}\right)+K_g(x_2)\,x_2 \\ & -K_s\left[\left(x_2-d_2\right)H\left(x_2-d_2\right)\right. \\ & \left.+\left(x_2+d_2\right)H\left(-x_2-d_2\right)\right]. \end{aligned} \tag{1}$$

where $H(\bullet)$ is the Heaviside unit step function; the displacement x_1' is expressed as a saturation function of x_1.

$$x_1'=\begin{cases} x_1-d_1, & \text{when } \dfrac{K_2}{K_1+K_2}x_2 < x_1-d_1, \\ x_1+d_1, & \text{when } \dfrac{K_2}{K_1+K_2}x_2 > x_1+d_1, \\ \dfrac{K_2}{K_1+K_2}x_2, & \text{others.} \end{cases} \tag{2}$$

The initial conditions of the rebounding spring and energy-buffering spring are x_{10} and x_{20}, respectively. These two initial conditions are correlated with the following relation

$$K_1x_{10}=K_2x_{20}. \tag{3}$$

The magnetic effect is taken as a nonlinear spring with negative stiffness, which is expressed as follows

$$K_g(x_2)\approx K_{g3}x_2^2+K_{g1}, \tag{4}$$

where K_{g3} and K_{g1} are two constants fitting the practical nonlinear magnetic force using the Duffing-type model. This polynomial approximation is valid in most cases. A more comprehensive model and the rationale for this simplification will be discussed in Section 3.2.

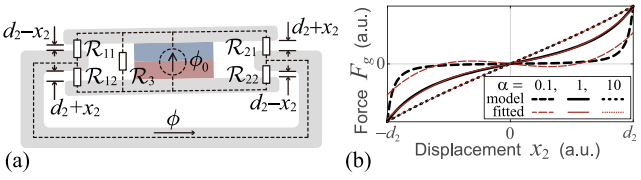

Fig. 3. Magnetic reluctance force model. (a) Equivalent magnetic circuit of the magnetic assembly. (b) Force and displacement relation of nonlinear stiffness K_g.

Combining the potential energies of the linear rebounding spring, linear energy-buffering spring, and nonlinear magnetic assembly yields the total potential energy of the QST system, which is expressed as follows

$$\begin{aligned} U(x_1,x_2) =& U_{K1}+U_{K2}+U_{Kg}+U_{Ks} \\ =& \frac{1}{2}K_1\left(x_1'+x_{10}\right)^2+\frac{1}{2}K_2\left(x_2-x_1'+x_{20}\right)^2 \\ & -\frac{1}{4}K_{g3}x_2^4-\frac{1}{2}K_{g1}x_2^2 \\ & +\frac{1}{2}K_s\left[\left(x_2-d_2\right)^2H\left(x_2-d_2\right)\right. \\ & \left.+\left(x_2+d_2\right)^2H\left(-x_2-d_2\right)\right]. \end{aligned} \tag{5}$$

There are two types of QST harvesters on the market, bistable and monostable ones, meeting different application requirements [13]. The bistable designs have no rebounding spring K_1, compared with the monostable ones; therefore, the two toggling positions are symmetric in positive and negative x_1 directions. On the other hand, the two toggling positions are both in the negative x_1 direction for the monostable design. The lumped model provided in Fig. 2 is compatible for modeling both cases by simply setting different stiffness values of K_1. The bistable case with zero K_1 is taken as a fundamental to discuss the potential energy variation during toggling operation in Section 3.3. The monostable design will be discussed in Section 3.5.

3.2. Magnetic reluctance force

The magnetic assembly, which facilitates the instantaneous magnetic poles swapping function, is one of the essential parts of the QST harvester. Fig. 3(a) shows the magnetic circuit of the assembly. ϕ_0 is the magnetic flux source provided by the permanent magnet. $\mathcal{R}_{11}$, $\mathcal{R}_{12}$, $\mathcal{R}_{21}$, and $\mathcal{R}_{22}$ represent the reluctance between the moving and fixed magnetic flux guiding iron bars. Their values are formulated as follows

$$\mathcal{R}_{11}=\mathcal{R}_{22}=\frac{d_2-x_2}{\mu_0\mu_rA};\quad \mathcal{R}_{12}=\mathcal{R}_{21}=\frac{d_2+x_2}{\mu_0\mu_rA}, \tag{6}$$

where μ_0 is the permeability of vacuum, μ_r is the relative magnetic permeability of the material (air in this study), and A is the cross-sectional area of the magnetic circuit in square meters. $\mathcal{R}_3$ models the reluctance due to the flux leakage. It is taken proportional to the constant gap $2d_2$ with a ratio α, i.e.,

$$\mathcal{R}_3=\alpha\left(\mathcal{R}_{11}+\mathcal{R}_{12}\right)=\frac{2\alpha d_2}{\mu_0\mu_rA}. \tag{7}$$

According to the basic magnetic circuit laws, the magnetomotive force (MMF) across the magnet can be formulated as follows

$$\mathcal{F}=\phi_0\left\{\mathcal{R}_3\|\left[\left(\mathcal{R}_{11}\|\mathcal{R}_{21}\right)+\left(\mathcal{R}_{12}\|\mathcal{R}_{22}\right)\right]\right\}. \tag{8}$$

The magnetic fluxes through $\mathcal{R}_{11}$ (same amount through $\mathcal{R}_{22}$) and $\mathcal{R}_{12}$ (same amount through $\mathcal{R}_{21}$) can be formulated as follows

$$\phi_{11}=\frac{\mathcal{F}}{2}\frac{\mathcal{R}_{21}}{\mathcal{R}_{11}+\mathcal{R}_{21}};\quad \phi_{12}=\frac{\mathcal{F}}{2}\frac{\mathcal{R}_{11}}{\mathcal{R}_{11}+\mathcal{R}_{21}}. \tag{9}$$

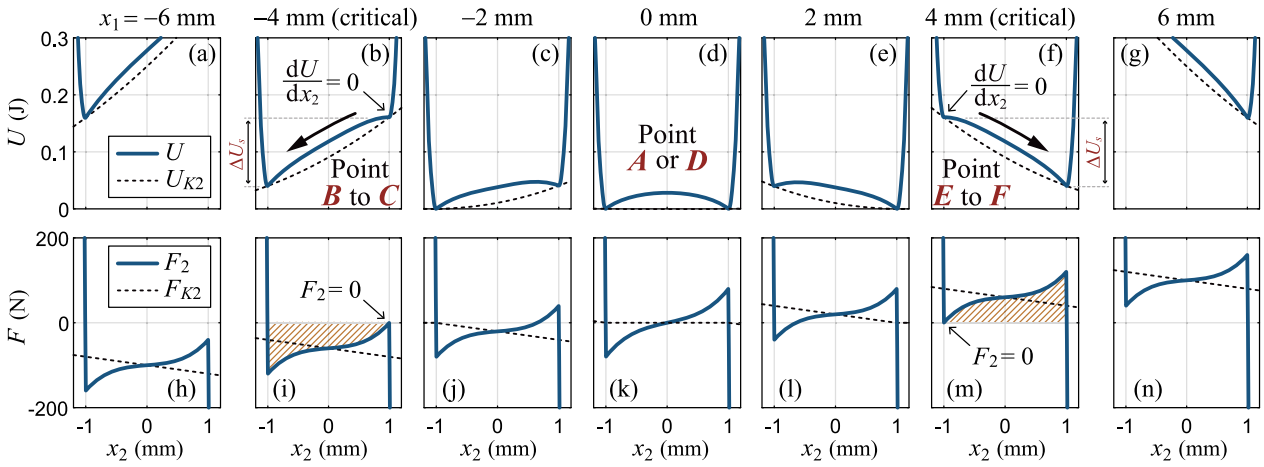

Fig. 4. The potential energy and force pictures as functions of x_2 at different excitation position x_1 under relatively soft K_2 and bistable (zero K_1) case.

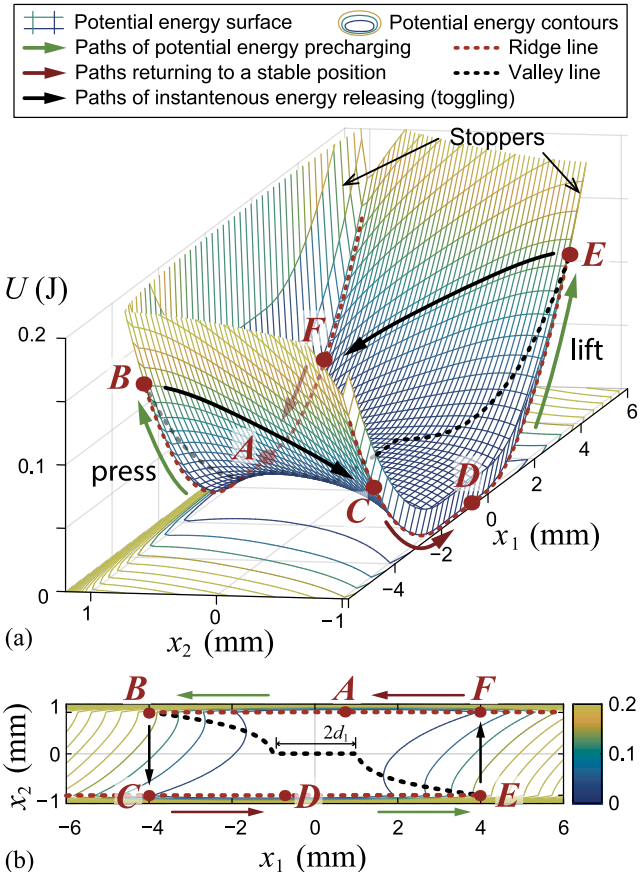

Fig. 5. The potential energy picture in one cycle of toggling actions under relatively soft K_2 and bistable (zero K_1) case. (a) Potential energy picture. (b) Potential energy contours.

Substituting (6) into (9) and referring to the reluctance force formula, the total reluctance force of the magnetic assembly can be expressed as a function of x_2, i.e.,

$$F_g(x_2) = 2(F_{11} + F_{12}) = -\phi_{11}^2 \frac{d\mathcal{R}_{11}}{dx_2} - \phi_{12}^2 \frac{d\mathcal{R}_{12}}{dx_2} = \frac{\alpha^2 \phi_0^2 d_2^3 x_2}{\mu_0 \mu_r A\left[(\alpha+1)d_2^2 - x_2^2\right]^2}. \tag{10}$$

Fig. 3(b) shows the functional relations between total reluctance force F_g and displacement x_2 under different reluctance ratio α, as well as their fitted curves with the quadratic polynomial nonlinear stiffness model provided in Eq. (4). Unlike a typical spring, which provides a restoring force, the magnetic force repels the mover away from the unstable equilibrium at the zero position. From Fig. 3(b), the Duffing-type model fits better when α is larger than 1. Deviations are more obviously found at small α. In that case, we had better rely on Eq. (10) rather than Eq. (4) to formulate the force produced by the magnetic assembly. In addition, the magnetic force calculated by Eq. (10) agrees with that generated by the "reluctance force actuator" block in Simulink, which is used in the dynamic simulation of Section 4.

3.3. Potential energy variation

Given the special magnetic assembly design, without external disturbance, the mover, i.e., node 2 in the equivalently lumped model shown in Fig. 2, must stop at either $x_2 = d_2$ or $-d_2$ position. Therefore, the magnetic assembly is a typical bistable structure. Potential energy analysis helps reveal its critical condition of toggling and the input mechanical energy at the firing instants. Since a quasi-static excitation is assumed in this paper, i.e., $\dot{x}_1 \to 0$, no kinetic energy is input to the system. Both F_2 [the total force at node 2, which is formulated in Eq. (1)] and U [the total potential energy of the system, which is formulated in Eq. (5)] are functions of the toggling point displacement x_2 and the action point displacement x_1. Their progressions with x_1 and x_2 elaborate the principle of QST energy harvesting.

The potential energy picture under a normally used soft precharging stiffness K_2 and bistable case is illustrated in Figs. 4 and 5 from different points of view. The parameters of the assembly are listed as the first case in Table 1. In this case, since $K_1 = 0$, there is no preloading force applied to K_2; therefore, the operation is symmetric with respect to the $x_1 = x_2 = 0$ vertical line. The potential energy 3D picture in a cycle of symmetrical toggling actions is illustrated in Fig. 5(a). It is kind of a special saddle surface, given the effect of positive stiffness along x_1 and local negative stiffness along x_2. The valley points and ridge points at different x_1 are connected into the valley and ridge lines and illustrated as the red and black dashed lines, respectively, in the figure. The valley lines (red) goes along the stoppers' positions, where $x_2 = \pm d_2$, while the ridge line (black) goes between $-d_2$ and d_2 as x_1 varies.

Starting from point A, one of the stable points, path A to B represents a press action ($x_1 < 0$), which precharges the energy-buffering spring K_2. When arriving at point B, the valley point merges with the ridge point. After that, there is no valley points when $x_2 = d_1$.

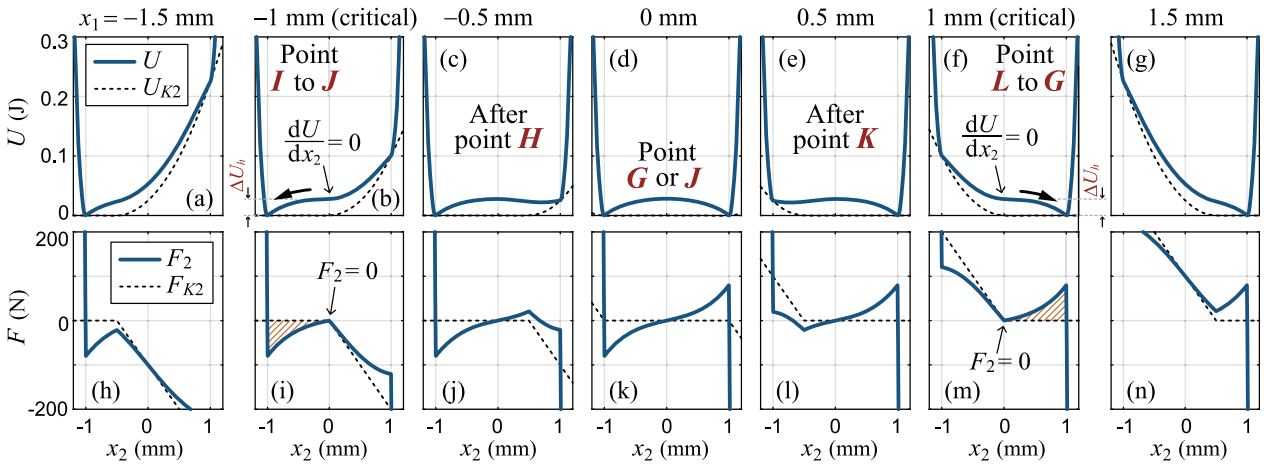

Fig. 6. The potential energy and force pictures as functions of x_2 at different excitation position x_1 under relatively hard K_2 and bistable (zero K_1) case.

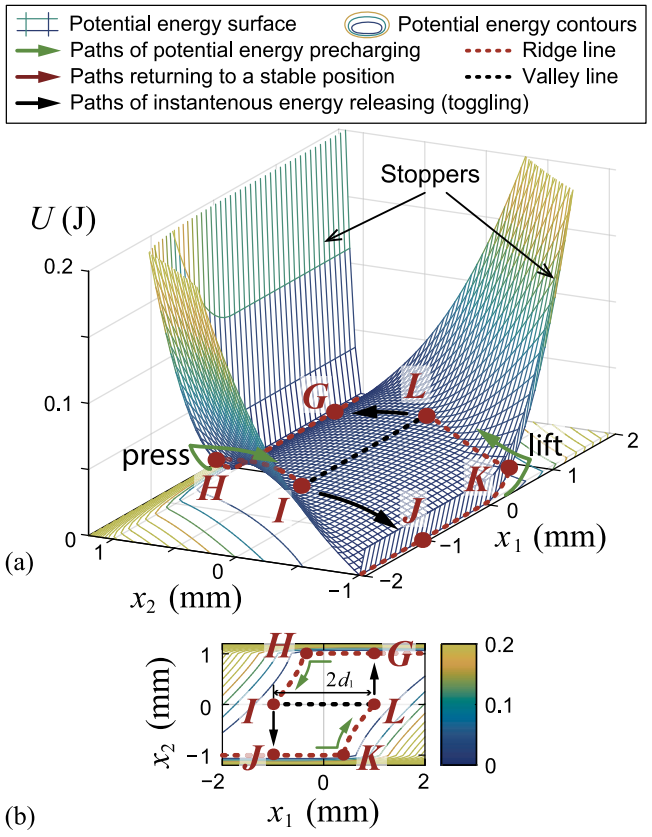

Fig. 7. The potential energy picture in one cycle of toggling actions under relatively hard K_2 and bistable (zero K_1) case. (a) Potential energy picture. (b) Potential energy contours.

It means after point B, the node 2 mover will immediately drop to point C, which toggles an instantaneous energy release at the critical x_1 position. The released energy is represented by the height difference between point B and C. After this toggling action, the mover stays at another stable point D, where the press action is finished. Likewise, the paths from point D to critical point E, and instantaneously to point F describe the toggling action in the other lifting direction ($x_1 > 0$). Such a toggling cycle can be further understood with the potential energy contours shown in Fig. 5(b). At either of the critical points B or E, the contour lines' tangent is perpendicular to the horizontal x_1 axis.

Table 1
Static parameters used in theoretical modeling (Section 3) and dynamic simulation (Section 4).

Case	Para.	Value	Para.	Value
Common parameter in three cases	K_{g1}	30 kN/m	d_1	1 mm
	K_{g3}	50 GN/m^3	d_2	1 mm
	K_s	10 GN/m		
Soft K_2, bistable (Section 3.3)	K_1	0	x_{10}	0
	K_2	20 kN/m	x_{20}	0
Hard K_2, bistable (Section 3.4)	K_1	0	x_{10}	0
	K_2	200 kN/m	x_{20}	0
Soft K_2, monostable (Section 3.5)	K_1	10 kN/m	x_{10}	−6 mm
	K_2	30 kN/m	x_{20}	−2 mm

Moreover, the $2d_1$ gap models the unidirectional constraint at either press or lift action.

Fig. 4(a)–(g) show several slices of the 3D pictures in Fig. 5(a) when x_1 varies around the equilibrium position. Fig. 4(h)–(n) show the pictures of the corresponding force F_2. F_2 is the sum of F_{K2}, F_{Kg}, and F_{Ks} as formulated in Eq. (1). Within these three forces, only F_{K2} is related to x_1. Therefore, moving x_1 acts as if introducing a translational up or down movement to the F_2 curve at $x_1 = 0$ condition, i.e., Fig. 4(k). Likewise, the picture of the total potential energy U under different x_1 can be regarded as a sum of the U curve at the $x_1 = 0$ case and a moving section of the parabolic curve of U_{K2}, as illustrated in Fig. 4(h)–(n). The conditions of critical x_1 positions are designated in Fig. 4(b), (f), (i), and (m). From the force pictures, the critical x_1 marks the transitional condition of F_2 from single to triple zero-crossing points. The released energy in each toggling action is denoted as ΔU_s in this soft K_2 bistable case, as illustrated in Fig. 4(b) and (f). Since U is the integral of F_2, when $K_1 = 0$, ΔU_s is proportional to the area, which is patterned by orange diagonals in Fig. 4(i) and (m).

The analysis of potential energy variation under different exciting position x_1 reveals the basic principle of the QST harvester in quasi-static operation. It is different from the existing dynamics and power analysis of bistable or snap-through structures. Almost all existing studies evaluate the power output under continuous excitation of different frequencies. In this paper, energy, rather than power, is considered the key factor in evaluating the energy harvesting performance. The MEH modules based on the QST mechanism have been manufactured and put into a successful business, such as motion-powered wireless switches, during the last two decades. Therefore, the QST mechanism is remarkable for MEH applications, even though it was ignored by people from academia until now.

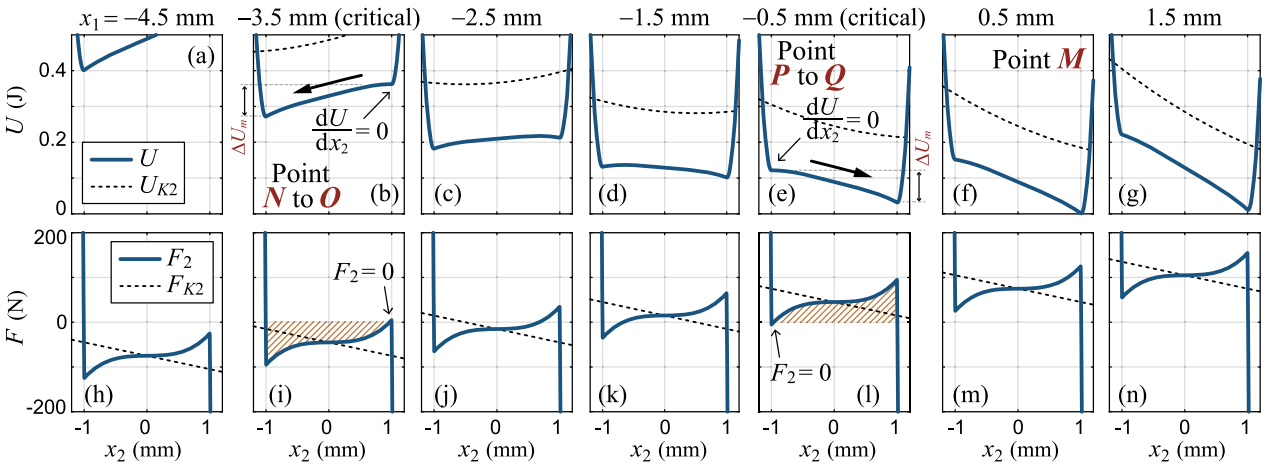

Fig. 8. The potential energy and force pictures as functions of x_2 at different excitation position x_1 under relatively soft K_2 and monostable (nonzero K_1) case.

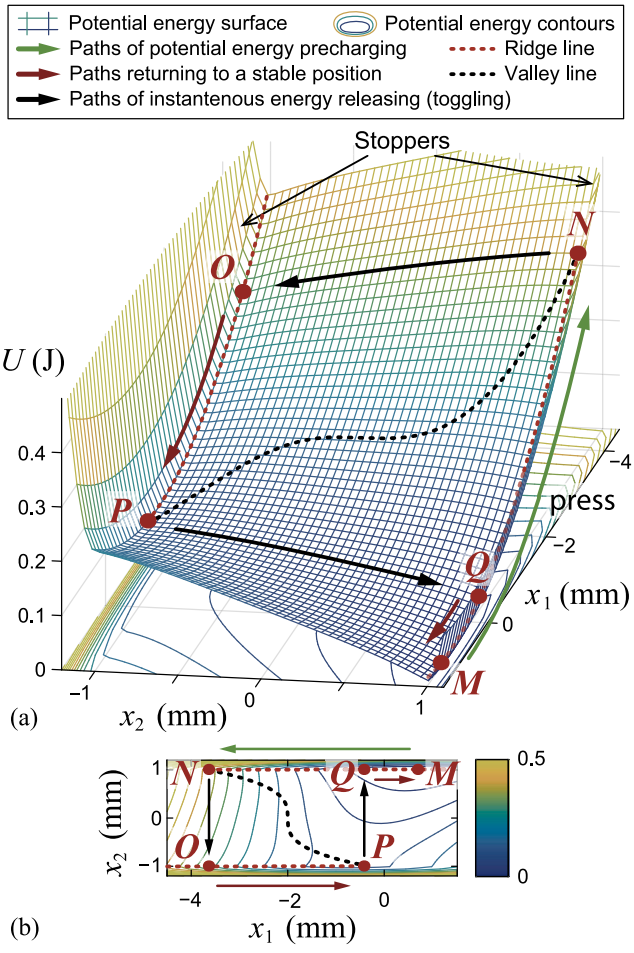

Fig. 9. The potential energy picture in one cycle of toggling actions under relatively hard K_2 monostable (nonzero K_1 and nonzero x_{10}) case. (a) Potential energy picture. (b) Potential energy contours.

3.4. Effect of energy precharging stiffness

In all QST products, the energy-buffering spring is a necessary component, e.g., the brass leaf spring in the EnOcean product shown in Fig. 1(a) [11]. This additional component can significantly increase the input mechanical energy in each toggling action. This subsection investigates the rationale behind this component.

When the energy-buffering spring is stiff, the potential energy picture looks different. The potential energy picture under a hard energy-buffering K_2 and the bistable case is illustrated in Figs. 6 and 7 from different points of view. The parameters are listed as the second case in Table 1. In this large K_2 case, the most obvious difference is that the valley lines are no longer confined in the $x_2 = \pm d_2$ positions, as we can observe from Fig. 7. The merging points of the valley lines and ridgeline are on the $x_2 = 0$ line. Therefore, when we press the QST harvester by starting from point G, the stable points diverge from the stopper position at $x_2 = d_2$ after passing point H and then instantaneously release the stored energy from $x_2 = 0$ to $-d_2$ (point I to point J), rather than from $-d_2$ to d_2 as those in the soft K_2 case. In the opposite lifting direction, the stable points diverge from the other stopper at $-d_2$ and the harvester travels from point L to point G to release the same amount of potential energy.

As we can observe from Fig. 5(b), the $2d_1$ gap is a necessity for enabling the sudden potential energy drops in this hard K_2 case. If the nonlinear term K_{g3} in the magnetic negative stiffness is small and can be neglected, the critical K_2 value distinguishing soft or hard features just equals to K_{g1}. In this case, we denote the released energy in each toggling action as ΔU_h, as illustrated in Fig. 6(b) and (d). ΔU_h is just the height of the potential barrier, which separates the bistable potential wells. Moreover, as we can observe from the patterned area in Fig. 6(i) and (m), which is proportional to the released energy, the area is much smaller than that in the soft K_2 case, which was shown in Fig. 4(i) and (m). If the nonlinear term K_{g3} is negligible, K_g can be regarded as a linear negative stiffness. Given the geometrical (approximately triangular) relation in the extreme very soft and very hard K_2 cases, we can have the following relation between the amounts of released energy in the two cases, i.e.,

$$\Delta U_s \approx 4\Delta U_h. \tag{11}$$

If the nonlinear K_{g3} term is significant, the enclosed area in Fig. 6(i) gets even smaller, while that in Fig. 4(i) remains the same; therefore, such an energy ratio might get even larger than four-folds. This explains the necessity of the soft energy buffering K_2 design in a practical product for realizing reliable and sufficient precharged potential energy.

3.5. Monostable design

Besides the bistable QST harvester module, the monostable version is also used in many self-powered switch scenarios [13]. In the monostable design, one toggling action happens on the way when the exciting rod is pressed down and the other happens on the way returning to its only stable position. To realize the monostable design, a preloaded

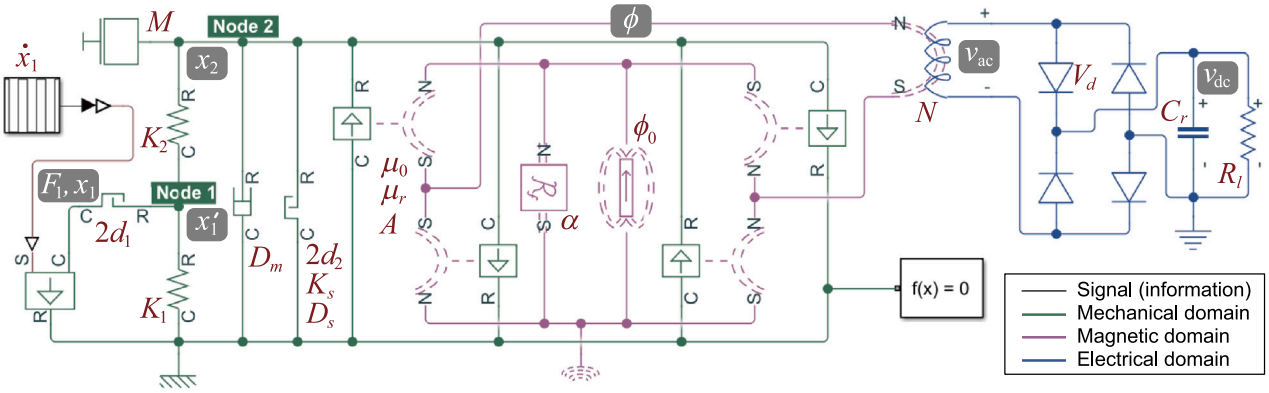

Fig. 10. Multifield coupled dynamic model for numeric simulation in Simulink.

rebounding spring K_1 connecting node 1 and the ground should be added.

The parameters used to study the monostable QST harvester are listed in the third case of Table 1. Figs. 8 and 9 show the potential energy picture of the monostable case. It should be noted that, after inserting nonzero K_1 and applying the preloading force, both the initial displacement of spring K_1 and K_2, i.e., x_{10} and x_{20} respectively, are negative. With a proper selection of the K_1 value, when excitation force is revoked, the node 2 mover can only rest at the $x_2 = d_2$ stable position, i.e., around point M in Fig. 8. When the QST harvester is pressed down, its potential energy goes along the green arrow line until attaining the critical point N, after which it drops to point O in a sudden. The mover is toggled from the $x_2 = d_2$ potential well to the $-d_2$ well. When the harvester is released from point O, its potential energy goes along the red arrow line. After another critical point P, the potential energy suddenly drops to point Q; the mover is toggled back to the d_2 potential well. In the monostable design, the gap of action point d_1 has no effect on the toggling actions since the force is only applied in the downward direction. The released energy in each toggling action is denoted as ΔU_m, as shown in Fig. 8(b) and (e).

In the datasheet of ZF bistable and monostable energy harvesters, the switch characteristics are explained with the force-travel diagrams [13]. Such diagrams might explain the behavior from the actuating point of view. However, they can explain neither the energy details nor the dynamic principle of a QST harvester. In fact, most of the previous QST products were developed based on empirical or trial-and-error engineering procedures. Without a rigorous theoretical study on the potential energy variation and toggling dynamics, in particular, those under the unique and useful quasi-static excitation condition, quantitative analysis and optimization toward more reliable, compact, and cost-effective designs are unable to be realized. Therefore, the potential energy analysis discussed in this section is necessary for this ultimate goal of optimal design.

4. Simulation of multifield dynamics

The theoretical energy analysis in Section 3 has provided a thorough understanding of the toggling principle and the amount of input mechanical energy in each toggling action. To further study the dynamics after each triggering point, we have to consider the dynamic components, such as mass M, mechanical damping D_m, and electrically induced damping D_e, as shown in Fig. 2.

Since the transient behavior after a toggling involves complex multifield coupled dynamics across the mechanical, magnetic, and electrical domains as well as some mechanical collisions at the stoppers, an analytical model with closed-form expressions is not easy to be developed right away. In this study, the multifield dynamics are numerically simulated with Simulink in Matlab. Fig. 10 shows the block diagram built in Simulink. The simulation model comprises mechanical components in green, magnetic components in magenta, and electrical components in blue. In the simulation model, four reluctance force actuator blocks linking the green mechanical and magenta magnetic domains are used to represent the reluctance components $\mathcal{R}_{11}$, $\mathcal{R}_{12}$, $\mathcal{R}_{21}$, and $\mathcal{R}_{22}$ in Fig. 3, whose values are related to the mechanical–magnetic interaction. The electromagnetic interaction during the toggling instants is modeled by the electromagnetic converter block, which links the magenta magnetic and blue electrical domains.

Table 2
Dynamic parameters used in dynamic simulation (Section 4).

Parameter	Value	Parameter	Value
ϕ_0	20 μWb	A	5 mm^2
μ_0	$4\pi \times 10^{-7}$ H/m	μ_r	1
M	100/10/1 g	D_m	1 N s/m
K_s	1×10^{10} N/m	α	π
D_s	1×10^{6} N s/m	C_r	1 mF
N	500 turns	V_d	0.6 V
R_l	100 MΩ		

Other quasi-static parameters in three study cases were listed in Table 1.

4.1. Simulation results

Following the three cases, whose static parameters were listed in Table 1 and energy pictures discussed in Section 3, we can further investigate the transient dynamic behavior of the QST harvester. The other dynamic parameters used in the dynamic simulation are illustrated in Fig. 10. Their values are listed in Table 2. Those dynamic parameters are kept the same in the three study cases. Fig. 11 shows the key waveform during the operation of the QST system under the three study cases.

4.1.1. Soft toggling bistable case

The key waveform of the soft toggling stiffness K_2 bistable case is shown in Fig. 11(a)–(f). As shown in Fig. 11(a1) and (a2), the activating node 1 displacement x_1 (dashed line) continuously and slowly varies between ±6 mm, such that to toggle the node 2 displacement x_2 (solid line) bistablly changing between ±1 mm, the stoppers positions. During the toggling moments, as shown in Fig. 11(c1) and (c2), the magnetic flux ϕ through the electromagnetic coil switches between the two stable values ϕ_0 and $-\phi_0$ almost in an instant. Through the N turns coil, voltage pulses are induced in the electrical domain, as shown by v_{ac} in Fig. 11(d1) and (d2). Through a diode bridge rectifier, whose forward

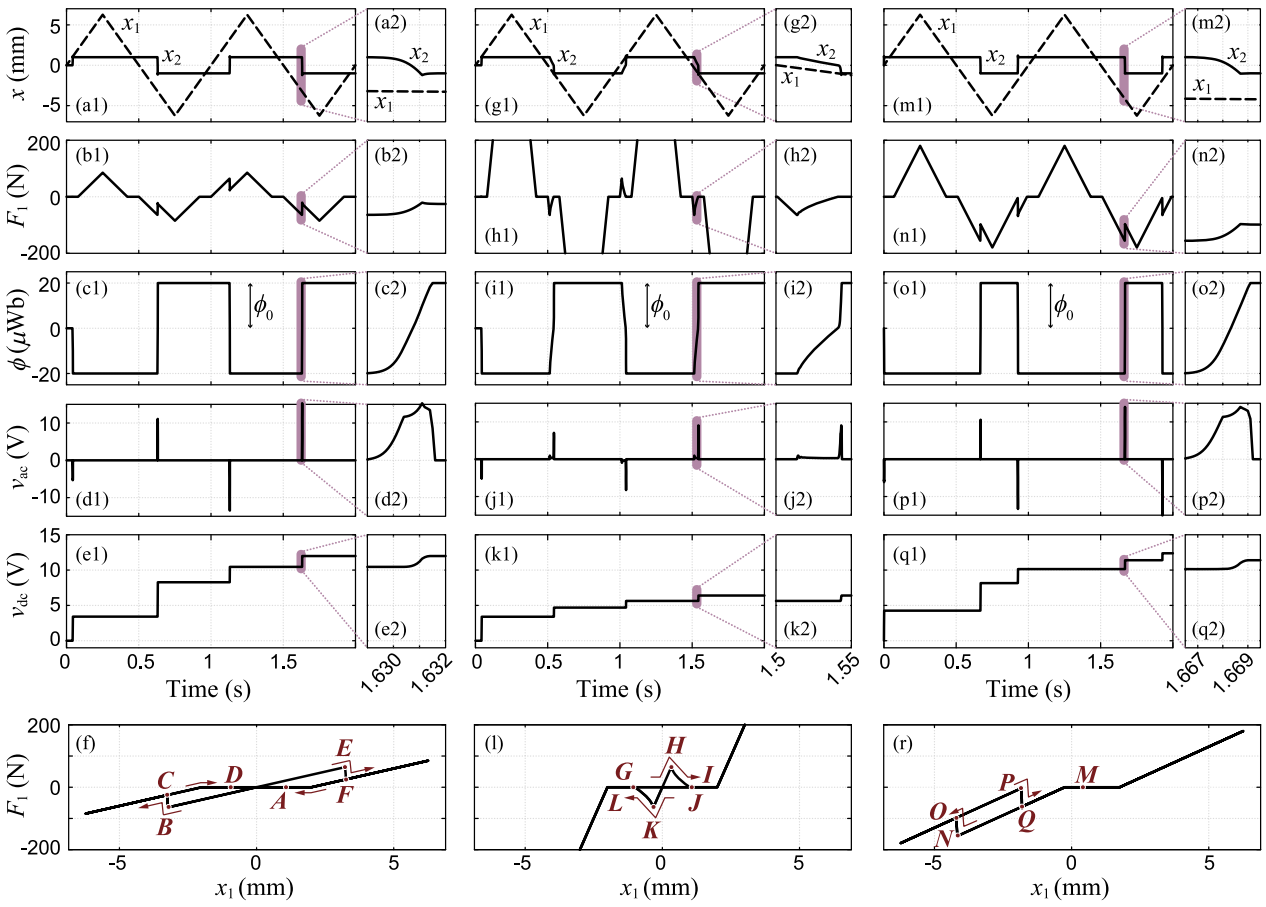

Fig. 11. Simulation results under three cases. (Parameters are provided in Tables 1 and 2. M = 1 g in this study). (a)–(f) Soft K_2 bistable case. (g)–(l) Hard K_2 bistable case. (m)–(r) Soft K_2 monostable case.

voltage drop is $2V_d$, and a filter capacitor C_r, the generated electricity is rectified into storable dc form, as shown by v_{dc} in Fig. 11(e1).

The toggling or actuating force at node 1, i.e., F_1 as illustrated in Fig. 11(b1), is also of interest for elaborating the toggling characteristics. It can be observed that F_1 abruptly drops at every toggling instant. Fig. 11(f) further illustrates the work cycle as a trajectory of the (x_1, F_1) points in every toggling cycle. The checkpoints from A to F correspond to the trajectory points shown in Fig. 5. Hysteresis is observed in this force–displacement figure. The enclosed area is proportional to the energy extracted from the QST system within one operation cycle [25].

4.1.2. Hard toggling bistable case

The key waveform of the hard toggling stiffness K_2 bistable case is shown in Fig. 11(g)–(l). As we can observe from the waveform of x_1 and x_2 in Fig. 11(g1) and (g2), the variations of x_2 in toggling actions are not as prompt as those in the soft K_2 cases. From the enlarged view shown in Fig. 11(g2), x_2 follows x_1 to slowly move for a d_2 distance before starting a sudden drop from the zero x_2 position. The observed phenomenon in numeric simulation agrees with that predicted in the theoretical analysis in Section 3.4. The degradation in toggling agility affects the magnetic flux changing speed and amount of generated energy. As shown in Fig. 11(j1) and (j2), the v_{ac} pulses have lower magnitude. The level of the output voltage v_{dc} after four toggling actions is only one-half of that in the soft K_2 case; therefore, the amount of energy stored in the capacitor C_r is only about one-fourth of that in the soft K_2 case, which approximately validates the theoretical prediction given in (11).

From the work cycle picture shown in Fig. 11(l), the area enclosed by the force–displacement trajectory is much smaller than that in the soft K_2 cases.

4.1.3. Soft toggling monostable case

The key waveform of the soft toggling stiffness K_2 monostable case is shown in Fig. 11(m)–(r). In the monostable case, the two toggling actions only take place in the negative x_1 range, one in the downward pressing process and the other in the upward releasing process. The toggling positions can be more obviously distinguished from the force F_1 waveform in Fig. 11(n1). The toggling positions can be tuned by adjusting the K_1 value and the initial deformations x_{10} and x_{20}. From Fig. 11(p1) and (p2), the generated voltage pulses during the toggling actions look approximately the same as those in the soft K_2 bistable case.

The monostable designs were extensively used in motion-powered switch applications as battery-free command transmitters. For one reason, only one pair of pressing and releasing actions gives two energy pulses; therefore, more energy is provided with one natural finger-press action. In the meanwhile, it also gives a better user experience. Given the possible packet loss in wireless communication, the physical position changes associated with bistable toggling actions might not be truthfully reflected in case of communication failure. On the other hand, the monostable design always returns to the reset position; no physical difference remains after every finger press-release action.

4.2. Effect of actuating gap $2d_1$

The actuating gap $2d_1$ is used to model the unidirectional force effect applied by the finger press or lift actions. Such a design is not necessary for the soft K_2 monostable case. As we can observe from Fig. 11(r), the hysteresis of force–displacement trajectory are all in the negative x_1 and negative F_1 region; it still works even if the positive

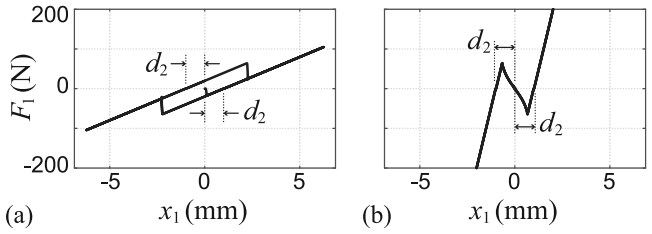

Fig. 12. The force–displacement trajectories under zero actuating gap ($d_1 = 0$) condition. (a) Soft K_2 bistable case. (b) Hard K_2 bistable case.

x_1 part is removed. For the soft K_2 bistable case, Fig. 12(a) shows the result under zero d_1 condition. It shows that it still works without inserting a nonzero $2d_1$ gap. The enclosed area, which corresponds to the extracted energy in one cycle, is approximated the same as that in the nonzero $2d_1$ condition. The balanced position of x_1, where $F_1 = 0$, is at $-d_2$ when $x_2 = -d_2$. It is at d_2 when $x_2 = d_2$.

For the hard K_2 case, the nonzero d_1 design is necessary. Fig. 12(b) shows the result with large K_2 under zero d_1 condition. Since node 2 is strongly confined by the rigid K_2 under both positive or negative $x_2 - x_1$ deformation, there is no abrupt displacement drop of x_2. No enclosed area is found in the force–displacement trajectory of Fig. 12(b); therefore, no energy can be extracted in the hard K_2 case, if not involving the nonzero d_1 model.

In real applications, the hard K_2 condition is seldom used, because of its inferior energy generation. But, in this study, understanding the underlying reason why soft K_2 is preferred, particularly the quantitative relation to the hard K_2 case, is of importance toward the fundamental principle and an all-rounded evaluation of the QST harvester.

4.3. Effect of toggling mass

The potential energy precharging can be carried out either very slowly or almost instantaneously, because the inertia of a real spring is very small, and therefore, can be neglected. But in the following energy-releasing stage, the equivalent mass M at node 2 matters. It confines how fast the mover of the magnetic assembly moves. Fig. 13 shows the selected waveform under three different toggling mass M in simulation. Comparing the three columns under different masses, we can find that a large mass impedes the rapid changes of x_2 between the two bistable positions $\pm d_2$ as well as the amount of magnetic flux ϕ between $\pm\phi_0$. Therefore, the induced voltage pulse has a smaller magnitude but wider span over time in a larger mass case. From these observations, we can conclude that, in general, smaller mass M is preferred, since it gives more rapid response and a larger electromotive force (EMF), or simply put, higher and easier-to-process voltage output.

4.4. Other issues in simulation

Besides the toggling mass M, there are some other dynamic components in Fig. 2 model. The mechanical damping D_m is mostly comprised of air damping during toggling. It is set to a very small value in simulation. The electrically induced damping D_e is implemented with a bridge rectifier as the interface circuit in this study, such that to show more details of the multifield coupled dynamics. The values of filter capacitance C_r and load resistance R_l can be adjusted to simulate different charging and loading effects. During each toggling action, the precharged energy is released in a burst. Only a portion of the released energy is converted into electricity through the electromagnetic coil. The remaining portion is dissipated in a mechanical collision at a stopper. The rigid contact of a stopper is modeled with a large stiffness K_s and a large contact damping D_s, whose values are listed in Table 2.

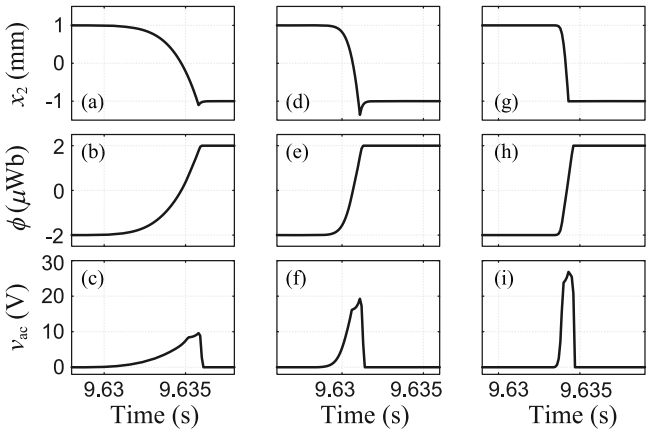

Fig. 13. Simulation results using different toggling mass. (a)–(c) $M = 100$ g. (d)–(f) $M = 10$ g. (g)–(i) $M = 1$ g.

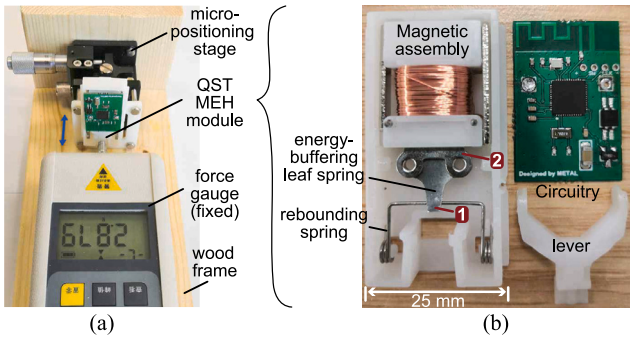

Fig. 14. Experimental setup (Video S1 showing its operation can be found in the online supplementary materials). (a) Testing setup. (b) Tested QST-MEH module manufactured by Chlorop Ltd. (mechanical assembly with an size of 25 × 45 × 10 mm^3) and METAL group at ShanghaiTech University (circuitry).

5. Experiments

The QST energy harvester module is a mature engineering product. It is used to build many commercial motion-powered switch products over the last two decades [11]. In this section, we take the measurement results from a QST harvester product, whose mechanical part is manufactured by Chlorop Ltd. from China, and electrical circuitry is developed by the authors' research group (METAL group at ShanghaiTech University in China), to validate the energy and dynamic analysis discussed in this paper.

5.1. Testing setup

Fig. 14(a) shows the experimental setup for measuring the quasi-static behavior and energy output of the QST harvester. The enlarged view of the QST-MEH module is shown in Fig. 14(b). The testing setup is composed of a force gauge and a manual micro-positioning stage, both of which are fixed on a wood frame. In the test, a QST-MEH module is mounted at the micro-positioning stage, while its actuating pedal is pressed by the measuring head of the force gauge. Because the manual micro-positioning stage travels extremely slow, manually rotating its tuning head one round only moves the stage by 0.5 mm, the actuating movement provides a rigorous quasi-static motion input. The quasi-static characteristics can be recorded by marking down the data pairs of the translational displacement and the corresponding pressing force.

To better show the necessity of the energy-buffering mechanism, two sets of data are recorded when the mover is actuated through an

Table 3
Equivalent component values identified from experimental data.

Parameter	Press at node 1 (soft K_2 mono.)	Press at node 2 (hard K_2 mono.)
K_1 (N/m)	1140	200
K_2 (N/m)	3380	40 000
ϕ_0 (μWb)	5.3	8.3
R_3 (1/H)	2×10^8	2×10^7
X_{20} (mm)	−1.2	−0.3
d_2 (mm)	0.92	0.55
M (kg)	0.2	0.2
D_m (N s/m)	1×10^{-5}	1×10^{-5}
N (turns)	500	500

K_s, D_s, μ_0, μ_r, A are the same as those listed in Table 2.

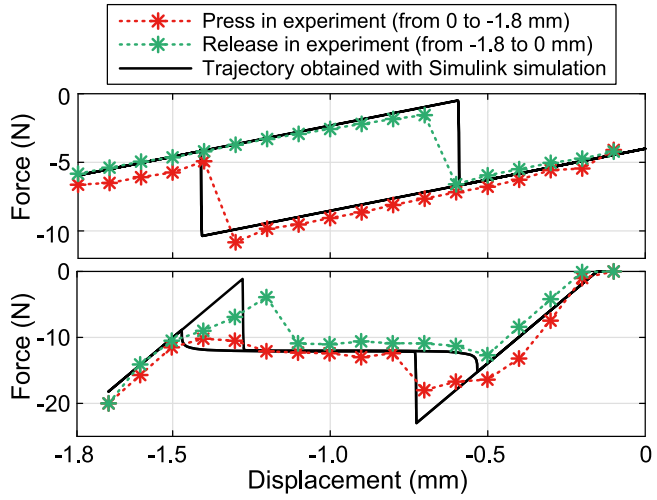

Fig. 15. Force–displacement trajectories in experiment and simulation comparison. (a) Soft K_2 monostable case (being pressed at node 1). (b) Hard K_2 monostable case (being pressed at node 2).

energy-buffering spring and a plastic lever, i.e., being pressed at node 1, or directly being pressed at the rigid node 2. The two pressing positions of the QST module are illustrated in Fig. 14(b).

5.2. Force–displacement trajectory

Fig. 15 shows the force–displacement trajectories when the QST module is pressed at node 1 (soft K_2 case) or 2 (hard K_2 case), respectively. The red and green discrete data points are measurement results obtained with the experimental setup. The black solid lines are simulation results, based on the component values, which are identified by fitting the experimental data points. The component values are listed in Table 3. Given the excitations at different actuating nodes, which also encounter different levering effects, all of the listed equivalent component values are not the same in the two cases. In general, the simulation results with these two parameter sets follow the experimental trajectories quite well. It validates the mechanical–magnetic–electrical model presented in Fig. 10 for simulating the multifield coupled dynamics of the QST-MEH device.

Some observations can be obtained from the two force–displacement trajectories. First, the soft K_2 case do release a larger amount of mechanical energy during each press-release cycle, as the enclosed area by the trajectory is larger. Second, the absolute input mechanical energy in one press-release cycle of the preferred soft K_2 case is about 5 N × 0.8 mm = 4 mJ. Knowing this absolute amount of energy is helpful for figuring out the possibility to make some specific sensing or computing demands in IoT applications. Given the conservation of energy, those continuous and impartible tasks whose total energy consumption is over this amount will never be fulfilled in any case, even with an ideal transducer and a perfect energy conversion and management circuit.

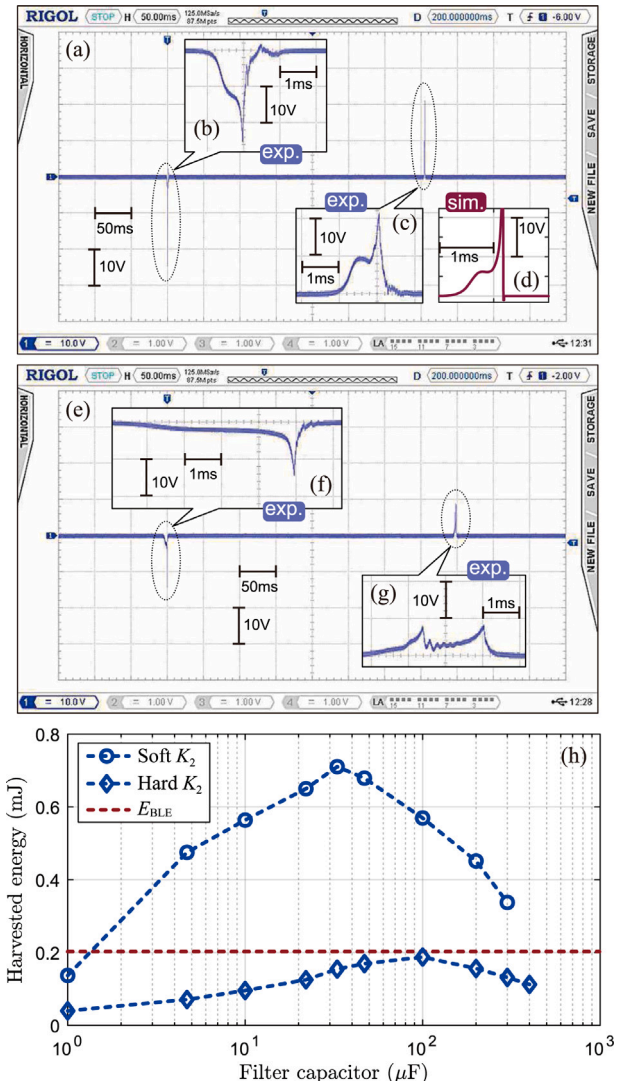

Fig. 16. Open-circuit voltage and harvested energy of the QST-MEH module in the experiment. (a)–(d) Soft K_2 case. (e)–(g) Hard K_2 case. (a) and (e) Overviews of a press-release cycle. (b) and (f) Enlarged views of the press-down moments in the experiment. (c) and (g) Enlarged views of the release moments in the experiment. (d) Enlarged views of a release moment in simulation. (h) Harvested energy under different values of filter capacitance in a press-release cycle.

5.3. Voltage and energy output

More measurement results of the open-circuit voltage (v_{ac} without the bridge rectifier, C_r, and R_l in Fig. 10) during the toggling instants under the aforementioned soft and hard K_2 monostable cases are shown in Fig. 16(a)–(g). Compared with the hard K_2 case, the preferred soft K_2 case outputs two higher and narrower voltage pulses in one press-release cycle, one negative and one positive pulses. From the enlarged views shown in Fig. 16(b) and (c), the duration and magnitude of a voltage pulse are about 1.5 ms and 20 V maximum, respectively, which is similar to those described in the datasheet of some QST switch products [11,13,14]. The pulsed voltage in the hard K_2 case lasts longer but has a smaller magnitude, as we can observe from the enlarged figures shown in Fig. 16(f) and (g). In addition, the voltage pulse profile recorded in simulation (Fig. 16(d)) looks very close to that of the experimental one (Fig. 16(c)). It once again validates the effectiveness

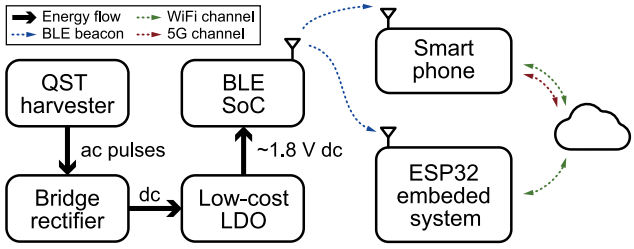

Fig. 17. IoT system architecture of the motion-powered BLE transmitters built with QST-MEH modules.

of the multifield coupled dynamic model provided in Fig. 10. The numerical model might be used for efficient parametric studies toward future optimal designs.

Besides the open-circuit output voltage, the energy harvesting performance is also investigated. The harvested energy under different filtering and storage capacitors C_r are shown in Fig. 16(h). Without the loading resistor R_l in Fig. 10, after a complete press-release action, the harvested energy is calculated as follows

$$E_h = \frac{1}{2} C_r V_{dc}^2, \tag{12}$$

where V_{dc} is the end dc voltage after the press-release action. From Fig. 16(h), the maximum harvested energy of the soft K_2 case is about 0.7 mJ, while that of the hard K_2 case is about 0.2 mJ. The ratio of output electrical energy in these two cases is about 3.5, which again shows a seemly correlating agreement with the four-fold relation of the input mechanical energy formulated in (11). To harvest maximum energy, an optimal filter capacitor should be selected. In this studying case, the optimal capacitance value is about 33 μF.

As this QST module can always give an energy output larger than 0.7 mJ, by adding some high-efficient circuit modules for voltage regulation and under-voltage lockout, it is convenient to design a low-energy application within this 0.7 mJ energy bound. For example, the energy consumption of a Bluetooth low-energy (BLE) beacon node, which was designed and optimized by the authors' research group, in sending one wireless packet is $E_{\mathrm{BLE}} \approx 0.2$ mJ [18], whose level is illustrated by the red dashed line in Fig. 16(h). Therefore, the QST-MEH-powered BLE beacon can send out two to three packets after each press-release action in applications.

5.4. IoT applications

Many designs have been proposed for motion or vibration energy harvesting during the last two decades. The major electromechanical transduction mechanisms being investigated include piezoelectric, electromagnetic, and electrostatic ones. In particular, the triboelectric nanogenerator (TENG), as one of the emerging realization electrostatic generators, has attracted a lot of research interest during the last decade [4,21]. On the other hand, from the industrial or engineering application point of view, in particular, for those designs targeting human-motion-powered electronics, *user experience* is a prior concern. For the motion-powered switch, there is a hard constraint for engineering applications that at least one wireless packet must be sent out after only one strike by either hand or foot, i.e., *one strike one packet* in short; otherwise, the user experience gets worse and even is regarded as unacceptable.

The QST-MEH module is a competent and mature product that can meet the aforementioned one strike one packet principle. As we can see in the measurement, the absolute input mechanical energy of each strike is at least 4 mJ; the converted and successfully harvested electrical energy is 0.7 mJ; while sending each BLE beacon packet consumes 0.2 mJ energy. Therefore, although there seems still a large space for potential improvement in electromechanical energy conversion efficiency, the 17.5% harvested energy, from mechanical input to optimal electrical output, can already reliably support the task of a motion-powered BLE beacon. According to the manufacturer's product specifications, these modules can properly work after millions of strikes [11]. Therefore, they are very robust.

Based on these QST-MEH modules and the circuitry design by our research group, we have prototyped several motion-powered IoT systems for the applications, such as interactive exhibitions, interactive toys, and self-powered sensing floor tiles for indoor positioning. The general architecture of these IoT systems is sketched in Fig. 17. The alternative current (ac) pulses generated by a QST module are rectified into direct current (dc) form, and then regulated into a constant dc output voltage around 1.8 V by a low-dropout (LDO) regulator, in order to power the digital system on a chip (SoC). By using the harvested energy, the SoC broadcasts some BLE beacon signals, which can be received by any BLE receivers such as smartphones or embedded systems in the vicinity, usually within 10 m. These pieces of information can finally reach the cloud servers through some WiFi or 5G network relays. Three application examples built based on this architecture are illustrated in Fig. 18. The corresponding videos (S2–S4) are provided in the supplementary materials. Given that these devices can send out two to three BLE beacon packets by pressing the 5 mm stroke QST buttons at whatever speed, they are very promising in building many practical battery-free and maintenance-free interactive products.

6. Discussion

Frequency up-conversion is an extensively discussed topic for low-frequency mechanical energy harvesting during the last decade. However, the slowest moving case, a quasi-static (excited by a very slow motion) energy harvester, was seldom reported and studied, even though they are a good fit with human-motion-powered battery-free devices, as demonstrated by the commercial QST harvester modules. The underneath reason might come from the extensively used but confusing term "kinetic energy harvesting". Most existing designs studied how to convert mechanical energy into electricity in real-time by implementing dynamic transducers, rather than using the first collect or store then release strategy. Power rather than energy has received more attention as a figure of merit for performance evaluation since most people considered continuously moving MEH systems. In fact, potential energy is as important as kinetic energy. They coexist in vibrations. Moreover, potential energy in a mechanical system has a unique feature, because it can be collected almost instantaneously with our everyday low-speed movements (given an input rod with small inertia) and steadily storable in a mechanical spring, etc. Existing renewable energy systems, such as hydro-power plants and compressed-air energy storage systems, also make use of potential energy as an intermediary form for energy collection and reservoirs. However, no sufficient attention was paid to potential energy as an intermediary energy form from the very beginning of the related research in small-scale MEH systems (around the 2000s).

A QST energy harvester and its associated power conversion and management circuit and embedded IoT module built a good example of a self-contained and self-sustaining battery-free wireless system. It realizes the most fundamental and critical design criteria of a practical battery-free IoT system, i.e., to commensurately satisfy the demand in sending a piece of useful information by making good use of the tiny amount of harvested energy. The most fantastic thing about the QST self-powered wireless switch is that it all happens with only one finger press.

Although the commercial QST-MEH modules have already provided a reliable way for realizing the "one strike one packet" motion-powered wireless BLE beacon, the current harvested electrical energy is only

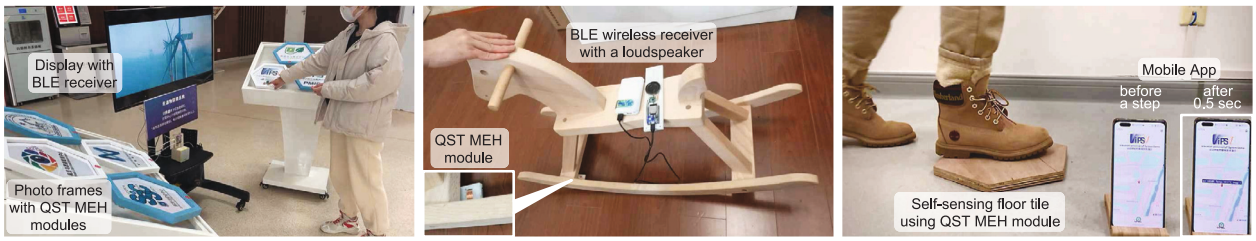

Fig. 18. Prototyped IoT applications using the motion-powered BLE transmitters built with QST-MEH modules (Video S2–S4 can be found in the online supplementary materials). (a) Interactive exhibition. (b) Interactive toy. (c) Self-powered sensing floor tile for indoor positioning.

17.5% of the input mechanical energy.[1] When the 0.7 mJ maximum harvested electrical energy is released in two 1.5 ms instants, the average power is up to 233.3 mW. Given that the size of the QST module is only 25 × 45 × 10 mm^3, the power over volume density after power conditioning during an instantaneous release in around 1.5 ms is up to 20.7 kW/m^3. If we skip the 10 mm thickness, the power over area density is 207 W/m^2, which is higher than many triboelectric designs [26–28]. In recent years, there has been extensive research interest in stretchable energy harvesters and self-powered sensors, etc., in particular, in those studies based on TENG [29–35]. Some of the studies on TENG reported a very high power density, say up to 2.67 kW/m^2 [36], more than 10 times of this QST MEH module. Yet, this power is recorded under a high-frequency or high rotational speed excitation (3 kHz in the 2.67 kW/m^2 case). As we know, TENG has a very high instantaneous power density; yet, the average power density is low. For example, a recent design has recorded an ultrahigh instantaneous power density of 10 MW/m^2 at a low frequency of about 1 Hz [37]; however, its average power density is only 790 mW/m^2, also at 1 Hz excitation. This average power density is 0.38% of that achieved by the QST module in this study. Moreover, the harvested energy by the QST module is ready-to-use energy in electrical dc form around a digital voltage level. It can supply power to the SoC after simple voltage regulation via a low-cost LDO. In this sense, the QST electromagnetic energy harvester is not only more efficient but also more mature than the emerging TENGs.

Referring to the first principle of mechanical energy, i.e., energy equals force multiples by displacement $E = F\Delta X$, the advantage of QST MEH module results from its relatively large impeding force against the movement. Such an impeding force always does negative work; therefore, input energy to the electromechanically coupled system. The magnitude of the pressing force to excite the QST module is about several N, as we can see from Fig. 15. Large force ensures the large input energy from the mechanical domain at a given travel distance. However, the force magnitudes of TENGs are usually at the mN levels [38], which is three orders of magnitude smaller than what a QST MEH module provides.

Future improvements of the QST MEH modules can be carried out to further increase the electromechanical energy conversion efficiency, cut down the power consumption in the power management process, and optimize the energy-aware computing routines. With those improvements in all mechanical, electrical, and cyber domains, future QST-MEH devices may either satisfy the same information demand with a lighter or unintentional finger press, or, in the other way round, acquire, process, and send out more pieces of useful information with a finger press at the similar strength. Starting from the quantification of energy supply and information demand, the energy analysis of the QST module provides a good example of systematic design by balancing the energy supply and information demand. The supply–demand balance principle and a synergistic design strategy across different disciplines must be emphasized in future designs and optimization.

[1] We can hardly find a published paper talking about the output energy over input energy conversion efficiency, because, in the past, most literature takes the functionality or power output as the figure of merit in evaluating the performance of an energy harvester.

7. Conclusion

The mechanical energy harvesting (MEH) modules manufactured by EnOcean GmbH et al. have been put into the successful business of motion-powered battery-free wireless switches for more than two decades. In this paper, for the first time, we provide rigorous energy and dynamic analysis of the physics of these quasi-static toggling (QST) MEH devices. The secrete of the QST operation includes the *slow potential energy accumulation* and the *sudden electromechanical energy transduction*. The potential energy and force pictures of different settings were carefully investigated based on a lumped mechanical model. In particular, the effect of the energy-buffering spring and the monostable design are emphasized. It turns out that, by properly designing the component parameters, we can manufacture the QST-MEH device with different dynamic features, which meet different user demands in practical battery-free applications. More attention should be drawn to the *potential energy precharging* mechanism, although it is well-known and classical in some sense, toward the effective and practical designs of MEH-based battery-free IoT systems.

CRediT authorship contribution statement

Shiyi Liu: Conceptualization, Methodology, Formal analysis, Data curation, Writing – original draft, Visualization. **Xin Li:** Software, Validation, Formal analysis, Visualization. **Li Teng:** Validation, Data curation, Visualization. **Guobiao Hu:** Methodology, Writing – review & editing. **Junrui Liang:** Conceptualization, Writing – review & editing, Investigation, Resources, Supervision, Project administration, Funding acquisition.

Declaration of competing interest

The authors declare that they have no known competing financial interests or personal relationships that could have appeared to influence the work reported in this paper.

Data availability

Data will be made available on request.

Acknowledgments

The authors appreciate Mr. Jianhua Lu, Mr. Zhihui Feng, Mr. Zibo He, and Mr. Chaoping He from Chlorop Ltd., Guangdong Province, China, for valuable discussions and comments about the design, manufacturing, and marketing information about the QST-MEH module; and also Mr. Jingying Chen and Mr. Cheng Tian from ShanghaiTech University for their coding efforts toward some applications in Section 5.4.

This work was supported in part by the Natural Science Foundation of Shanghai, China under Grant 21ZR1442300; in part by the National Natural Science Foundation of China under Grants 62271319 and U21B2002.

Appendix A. Supplementary data

Supplementary material related to this article can be found online at https://doi.org/10.1016/j.nanoen.2022.107887.

References

[1] M. Safaei, H.A. Sodano, S.R. Anton, A review of energy harvesting using piezoelectric materials: state-of-the-art a decade later (2008–2018), Smart Mater. Struct. 28 (11) (2019) 113001.
[2] Liang, Li, Yang, Kinetic energy harvesting toward battery-free IoT: Fundamentals, co-design necessity and prospects, ZTE Commun. (2021).
[3] Z. Yang, S. Zhou, J. Zu, D. Inman, High-performance piezoelectric energy harvesters and their applications, Joule 2 (4) (2018) 642–697.
[4] J. Chen, Z.L. Wang, Reviving vibration energy harvesting and self-powered sensing by a triboelectric nanogenerator, Joule (2017).
[5] H. Fu, X. Mei, D. Yurchenko, S. Zhou, S. Theodossiades, K. Nakano, E.M. Yeatman, Rotational energy harvesting for self-powered sensing, Joule (2021).
[6] X. Li, G. Hu, Z. Guo, J. Wang, Y. Yang, J. Liang, Frequency up-conversion for vibration energy harvesting: A review, Symmetry 14 (3) (2022) 631.
[7] S. Zhou, J. Cao, A. Erturk, J. Lin, Enhanced broadband piezoelectric energy harvesting using rotatable magnets, Appl. Phys. Lett. 102 (17) (2013) 173901.
[8] H. Fu, E.M. Yeatman, Effective piezoelectric energy harvesting using beam plucking and a synchronized switch harvesting circuit, Smart Mater. Struct. 27 (8) (2018) 084003.
[9] S. Fang, X. Fu, X. Du, W.-H. Liao, A music-box-like extended rotational plucking energy harvester with multiple piezoelectric cantilevers, Appl. Phys. Lett. 114 (23) (2019) 233902.
[10] Z. Wang, W. Liu, W. He, H. Guo, L. Long, Y. Xi, X. Wang, A. Liu, C. Hu, Ultrahigh electricity generation from low-frequency mechanical energy by efficient energy management, Joule (2021).
[11] EnOcean, ECO 200 energy harvester datasheet, 2021.
[12] F. Schmidt, Electromagnetic energy transducer (US patent), 2012.
[13] Z. GmbH, Bistable energy harvesting generator for RF switches (datasheet), 2016.
[14] ALPS Electronic Co. Ltd., User manual for alps energy harvester SPGA series, 2018.
[15] Wuhan Linptech Co., Ltd, https://www.linptech.org/.
[16] Shunde Chlorop Co., Ltd, http://www.chlorop.com/.
[17] R.L. Harne, K.W. Wang, A review of the recent research on vibration energy harvesting via bistable systems, Smart Mater. Struct. 22 (2) (2013) 023001.
[18] X. Li, H. Tang, G. Hu, B. Zhao, J. Liang, ViPSN-Pluck: A transient-motion-powered motion detector, IEEE Internet Things J. 9 (5) (2022) 3372–3382.
[19] S. Liu, A.I. Azad, R. Burgueño, Energy harvesting from quasi-static deformations via bilaterally constrained strips, J. Intell. Mater. Syst. Struct. 29 (18) (2018) 3572–3581.
[20] P. Jiao, Y. Yang, K.I. Egbe, Z. He, Y. Lin, Mechanical metamaterials Gyro-Structure piezoelectric nanogenerators for energy harvesting under Quasi-Static excitations in ocean engineering, ACS Omega 6 (23) (2021) 15348–15360.
[21] Z.L. Wang, L. Lin, J. Chen, S. Niu, Y. Zi, Triboelectric Nanogenerators, Springer, 2016.
[22] J. Zhao, G. Zhen, G. Liu, T. Bu, W. Liu, X. Fu, P. Zhang, C. Zhang, Z.L. Wang, Remarkable merits of triboelectric nanogenerator than electromagnetic generator for harvesting small-amplitude mechanical energy, Nano Energy 61 (2019) 111–118.
[23] J. Liang, W.H. Liao, Impedance modeling and analysis for piezoelectric energy harvesting systems, IEEE/ASME Trans. Mechatron. 17 (6) (2012) 1145–1157.
[24] J. Liang, H.S.-H. Chung, W.-H. Liao, Dielectric loss against piezoelectric power harvesting, Smart Mater. Struct. 23 (9) (2014) 092001.
[25] J. Liang, W.-H. Liao, Energy flow in piezoelectric energy harvesting systems, Smart Mater. Struct. 20 (1) (2010) 015005.
[26] L. Zhou, D. Liu, L. Liu, L. He, X. Cao, J. Wang, Z.L. Wang, Recent advances in self-powered electrochemical systems, Research 2021 (2021) 4673028.
[27] Z. Zhao, Y. Dai, S.X. Dou, J. Liang, Flexible nanogenerators for wearable electronic applications based on piezoelectric materials, Mater. Today Energy 20 (2021) 100690.
[28] L. Zhou, D. Liu, J. Wang, Z.L. Wang, Triboelectric nanogenerators: Fundamental physics and potential applications, Friction 8 (3) (2020) 481–506.
[29] Y. Wu, Y. Li, Y. Zou, W. Rao, Y. Gai, J. Xue, L. Wu, X. Qu, Y. Liu, G. Xu, L. Xu, Z. Liu, Z. Li, A multi-mode triboelectric nanogenerator for energy harvesting and biomedical monitoring, Nano Energy 92 (2022) 106715.
[30] N. Sezer, M. Koç, A comprehensive review on the state-of-the-art of piezoelectric energy harvesting, Nano Energy 80 (2021) 105567.
[31] R.A. Surmenev, R.V. Chernozem, I.O. Pariy, M.A. Surmeneva, A review on piezo- and pyroelectric responses of flexible nano- and micropatterned polymer surfaces for biomedical sensing and energy harvesting applications, Nano Energy 79 (2021) 105442.
[32] Shi, He, Lee, More than energy harvesting–combining triboelectric nanogenerator and flexible electronics technology for enabling novel micro-/nano-systems, Nano Energy (2019).
[33] C. Zhang, H. Chen, X. Ding, F. Lorestani, C. Huang, B. Zhang, B. Zheng, J. Wang, H. Cheng, Y. Xu, Human motion-driven self-powered stretchable sensing platform based on laser-induced graphene foams, Appl. Phys. Rev. 9 (1) (2022) 011413.
[34] H. Zhou, Y. Zhang, Y. Qiu, H. Wu, W. Qin, Y. Liao, Q. Yu, H. Cheng, Stretchable piezoelectric energy harvesters and self-powered sensors for wearable and implantable devices, Biosens. Bioelectron. 168 (2020) 112569.
[35] S. Zhang, J. Zhu, Y. Zhang, Z. Chen, C. Song, J. Li, N. Yi, D. Qiu, K. Guo, C. Zhang, T. Pan, Y. Lin, H. Zhou, H. Long, H. Yang, H. Cheng, Standalone stretchable RF systems based on asymmetric 3D microstrip antennas with on-body wireless communication and energy harvesting, Nano Energy 96 (2022) 107069.
[36] C. Han, C. Zhang, W. Tang, X. Li, Z.L. Wang, High power triboelectric nanogenerator based on printed circuit board (PCB) technology, Nano Res. 8 (3) (2015) 722–730.
[37] H. Wu, S. Wang, Z. Wang, Y. Zi, Achieving ultrahigh instantaneous power density of 10 MW/m2 by leveraging the opposite-charge-enhanced transistor-like triboelectric nanogenerator (OCT-TENG), Nature Commun. 12 (1) (2021) 1–8.
[38] G. Xu, X. Li, X. Xia, J. Fu, W. Ding, Y. Zi, On the force and energy conversion in triboelectric nanogenerators, Nano Energy 59 (2019) 154–161.

Shiyi Liu received the B.Eng. degree in Mechanical Engineering from the University of Michigan and Shanghai Jiao Tong University Joint Institute in 2021. She is currently pursuing her Master's degree at the School of Information Science and Technology, ShanghaiTech University. Her research interests include big data visualization and visual analytics, battery-free IoT, and mechanical energy harvesting.

Dr. Xin Li received the B.Eng. and B.Econ. degrees from the North University of China in 2016 and the Ph.D. degree from a joint program of the Chinese Academy of Science and ShanghaiTech University, Shanghai, China in 2021. He is now an Associate Professor with the Guangzhou Institute of Technology, Xidian University, China. His research interests include kinetic/vibration energy harvesting, intermittent computing, ubiquitous computing, and the Internet of Things.

Li Teng received his B.Eng. degree in Microelectronics from Hefei University of Technology in 2015. From 2015 to 2016 he worked as an analog IC design engineer in Wuxi ETEK Microelectronics Co., Ltd. He is now working toward a Ph.D. degree at ShanghaiTech University. His research interests include low-power management circuits and analog/mixed-signal IC design.

Dr. Guobiao Hu received the B.Eng. degree from Southwest Jiaotong University, Chengdu, China, in 2012, the Diplôme d'Ingénieur from École Centrale Paris, Châtenay-Malabry, France, in 2015, and the Ph.D. degree from the University of Auckland, Auckland, New Zealand, in 2020. He is currently a tenure-track Assistant Professor with the Internet of Things Thrust, Information Hub, The Hong Kong University of Science and Technology (Guangzhou), China. His research interests include vibration/wind energy harvesting and acoustic-elastic metamaterials.

Dr. Junrui Liang received the B.Eng. and M.Eng. degrees in Instrumentation Engineering from Shanghai Jiao Tong University, Shanghai, China, in 2004 and 2007, respectively, and the Ph.D. degree in mechanical and automation engineering from The Chinese University Hong Kong, China in 2010. He is currently an tenured Associate Professor with the School of Information Science and Technology, ShanghaiTech University, China. His research interests include energy conversion and power conditioning circuits, kinetic energy harvesting and vibration suppression, battery-free IoT, and mechatronics.